surfaces

MDPI

Article

Studying the Photoactivity of Ag-Decorated TiO_2 Nanotubes with Combined AFM and Raman Spectroscopy

Manjunath Veeranna Shinnur [1], Marco Menegazzo [2], Gianlorenzo Bussetti [2,*], Lamberto Duò [2], MariaPia Pedeferri [1] and Maria Vittoria Diamanti [1]

[1] Department of Chemistry, Materials and Chemical Engineering "Giulio Natta", Politecnico di Milano, Via Mancinelli 7, 20131 Milano, Italy; manjunathveeranna.shinnur@polimi.it (M.V.S.); mariapia.pedeferri@polimi.it (M.P.); mariavittoria.diamanti@polimi.it (M.V.D.)

[2] Department of Physics, Politecnico di Milano, p.za Leonardo da Vinci 32, 20133 Milano, Italy; marco.menegazzo@polimi.it (M.M.); lamberto.duo@polimi.it (L.D.)

* Correspondence: gianlorenzo.bussetti@polimi.it; Tel.: +39-0223996133

Abstract: The drive for the development of systems that can simultaneously investigate chemical and morphological information comes from the requisite to fully understand the structure and chemical reactivity relationships of materials. This is particularly relevant in photocatalysis, a field ruled by surface interactions. An in-depth understanding of these complex interactions could lead to significant improvements in materials design, and consequently, in photocatalytic performances. Here, we present a first approach to a combined atomic force microscopy (AFM) and Raman spectroscopy characterization of anodic TiO_2 nanotubes arrays decorated with Ag nanoparticle electrodeposition from either the same anodizing organic electrolyte or from an aqueous one. Photocatalytic substrates were used in up to 15 consecutive photocatalysis tests to prove their possible deterioration with reuse. Sample aging can, in principle, produce changes in both the morphology and the chemical compounds that characterize the photocatalyst surface. Adopting multiple characterization techniques, such as a combination of AFM and Raman spectroscopy in an original setup, can profitably enable the observation of surface contamination. A significant drop in photocatalytic activity was observed after 10 cycles on samples where silver was deposited from the organic electrolyte, while the others remained stable. Such a drop was ascribed to photocatalyst deactivation. While in other cases, a simple recovery treatment allowed the initial photoactivity to be restored, this deactivation was not restored even after chemical and thermal cleaning treatments.

Keywords: TiO_2 nanotubes; Ag nanoparticles; photocatalysis; rhodamine-B; deactivation; atomic force microscopy (AFM); Raman spectroscopy; chemical maps

check for updates

Citation: Shinnur, M.V.; Menegazzo, M.; Bussetti, G.; Duò, L.; Pedeferri, M.; Diamanti, M.V. Studying the Photoactivity of Ag-Decorated TiO_2 Nanotubes with Combined AFM and Raman Spectroscopy. *Surfaces* **2024**, *7*, 938–950. https://doi.org/10.3390/surfaces7040061

Academic Editors: Gaetano Granozzi and Tomasz Kosmala

Received: 26 September 2024
Revised: 23 October 2024
Accepted: 30 October 2024
Published: 2 November 2024

1. Introduction

Titanium dioxide (TiO_2) is an n-type semiconductor and one of the most studied photocatalysts. Its popularity is due to its excellent chemical stability, natural formation, high resistance to photocorrosion, low toxicity, and thermal stability [1–3]. Due to its light absorption ability, TiO_2 has important applications in the fields of photocatalysis and photovoltaics. However, TiO_2 has some limitations. In particular, a band gap greater than 3 eV limits light absorption at ultraviolet wavelengths. This accounts for only a small fraction of the total solar spectrum and leads to the rapid coupling of photogenerated charge carriers [4].

Many strategies have been developed to solve these problems, such as doping TiO_2 with noble metals such as Ag and Au. Isolated impurities can introduce absorption defect states and reduce the recombination rate by trapping one carrier and freeing the other one to escape. Although these strategies reduce losses due to the lower number of initial carriers, the bandgap of TiO_2 remains in the UV region [5,6]. Enhancement mechanisms, such as plasmon-induced charge or energy transfer and photon scattering, have shown promise in semiconductor/plasmonic photocatalysis. These mechanisms are facilitated by the localized surface plasmon resonance (LSPR) properties of metal nanoparticles (NPs), which provide significant advantages for photocatalysis by reducing the recombination rate and expanding the spectral absorption range of the material [7,8]. Additionally, plasmonic noble metal NPs exhibit surface-enhanced Raman scattering (SERS) effects, which enable the sensitive Raman spectral detection of organic compounds, and their integration into TiO_2 nanostructured arrays as support for loading NPs significantly increases the sensitivity and reproducibility of the SERS effect [9,10]. Indeed, the chemical mechanism at the semiconductor/metal interface enhances both the strength and sensitivity of SERS, thereby enhancing the photocatalytic performance in addition to the SERS ability. The results of loading Ag to TiO_2 have shown promising results for photocatalytic applications, with the optimized Ag content increasing the photodegradation efficiency [11,12].

In this context, surface characterization plays a key role in understanding interactions and reactions. Correlating morphological and chemical information may lead to important steps toward the understanding and improvement of photocatalytic materials [13]. The surface morphology of an electrode can currently be investigated by atomic force microscopy (AFM) systems both in air and inside an electrolyte (in situ AFM). In fact, if the electrolyte is transparent in the visible energy region, traditional AFM setups where the cantilever deflection is monitored by a laser beam focused on the back of the tip can be employed. Some information can be inferred from force curves collected with AFM in the dynamic mode. Specifically, in the case of TiO_2, the hydroxylation level can be observed, which is strictly related to its photocatalytic activity [14]. Still, AFM cannot be the first choice when a detailed chemical analysis of the surfaces is required.

To overcome this difficulty, a combination of spectroscopic techniques is generally useful. Among the possible choices, Raman spectroscopy has attracted the interest of many researchers because it is able to identify chemical compounds on the surface by detecting the diffused light produced by a laser beam focused on the sample by an objective. Obviously, the lateral resolution of Raman spectroscopy is limited by light diffraction, while AFM is affected by the tip radius, which is typically some tens of nanometers. Nowadays, tip-enhanced Raman spectroscopy (TERS) can shift the lateral resolution to its limit by employing the AFM tip as a nano-source of light [15]. However, TERS application in an electrochemical cell is not easy and, for the moment, limited to some specific cases [16]. This is what led us to develop an original setup that combines AFM and traditional Raman spectroscopy for measurements both in air and inside an electrolyte. This system is described in [17], and we expose its principle of operation in the next paragraph. Here, we show its application in a case study that may open the way to the characterization of photocatalytic devices. In this first investigation, we focused on the stability and photocatalytic efficiency of the synthesized photocatalysts that were used in the photocatalytic degradation of rhodamine B (Rh-B) in aqueous solution under UV light for multiple cycles. One of the photocatalysts was thoroughly rinsed after every cycle while the other was left uncleaned to examine how morphological modifications and adsorbed molecules affected the photocatalyst stability and photocatalytic effectiveness. Integrating photocatalytic efficiency evaluation with molecular and morphological data provided by AFM and Raman should better explain how surface characteristics impact the material's overall performance.

2. Materials and Methods

2.1. Photocatalyst Preparation

TiO_2 nanotube synthesis was achieved through the electrochemical anodization technique. First, titanium sheets with a thickness of 0.5 mm were cut into square foils of 1 cm × 1 cm. They were then extensively cleaned in an ultrasonic bath with acetone and ethanol, and then deionized water for ten minutes each. Compressed air was then used to dry the Ti foils. To increase the homogeneity of the nanotube structure, we employed a two-step anodizing procedure [18]. The samples were anodized at 45 V for 30 min in potentiostatic conditions (Potentiostat LTC-Caoduro) in ethylene glycol containing 0.2 M

NH_4F and 2 M H_2O in, as reported in previous studies [19,20]. Following the first anodization, sonication in ethanol and deionization (DI) in water for ten minutes each was used to remove the grown TiO_2 nanotube (TNT) layer. Under the same electrolyte and potentiostatic conditions as in the first step, a second anodization was carried out on the pre-patterned titanium sheet generated from the first anodization. To eliminate any leftover electrolytes, the samples were rinsed with water and ethanol following the same process. After that, the samples were annealed for 2 h at 450 °C (GEFRAN 1200 oven).

Electrochemical deposition was employed to decorate Ag nanoparticles on the obtained TiO_2 nanotubes in two ways, as follows:

(1) In aqueous solution containing 5 mM $AgNO_3$ and 0.1 M Na_2SO_4 as the electrolyte. The deposition conditions were 20 mA/cm^2 for 1 min under galvanostatic conditions (AimTTi PLH120-P DC power supply)—labelled A.

(2) In organic solution containing 10 mM $AgNO_3$ in ethylene glycol as the electrolyte. The deposition conditions were 5 V for 1 min under potentiostatic conditions—labelled O.

After deposition, the samples were thoroughly rinsed in deionized (DI) water and dried in air. Two samples were produced for each condition; one was cleaned (C) following each photocatalytic cycle, while the other was left uncleaned (UC). A schematic representation of the synthesis of Ag nanoparticle-electrodeposited TNT is shown in Figure 1.

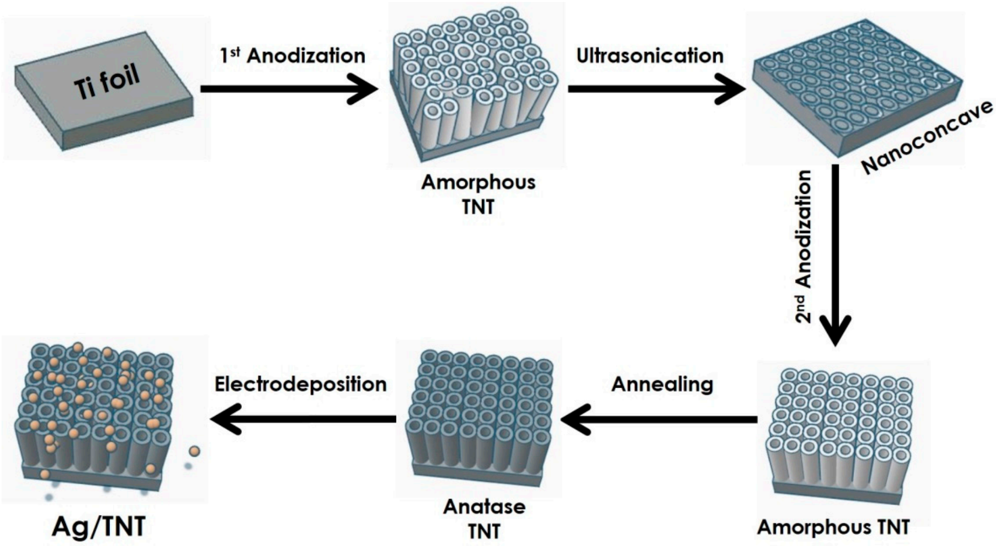

Figure 1. Schematic representation of the process for synthesizing Ag NP-electrodeposited TNT photocatalysts.

2.2. Photocatalysis Measurements

Photocatalytic experiments were carried out using mini-batch photoreactors consisting of a beaker containing 40 mL of organic dye solution (5×10^{-6} M aqueous Rh-B) and a stirring system to ensure homogenization of the dye concentration in the solution and oxygen flow to the photocatalyst surface. Each photocatalyst was placed horizontally in the solution, and UV light was irradiated using a UV-A LED (Nichia NCSU033B, peak power of 365 nm, UV-A intensity of 11.1 mW/cm^2) placed at a distance of 3 cm from the photocatalyst. The photocatalytic efficiency of the samples was evaluated by measuring the absorbance values of the dye solution every hour at 555 nm using a vis-spectrophotometer (SPECTRONIC 200E, Thermo Fisher Scientific, Les Ulis, France).

To examine the photocatalyst stability and investigate the effect of the cleaning process on efficiency, 10 photocatalytic cycles (n) were carried out under the same conditions, and the samples were either cleaned (C) or not cleaned (UC) with ethanol and DI water between one cycle and the following.

2.3. Photocatalyst Regeneration

To restore the photocatalytic performance of photocatalyst O_UC_10, three different regeneration processes were carried out.

The first one relied on UV regeneration. The photocatalyst was put in the batch reactors with 40 mL of deionized water and coupled to a stirring mechanism under UVA light. Following a 24 h period, the photocatalyst was dried in air.

The second method was thermal. The photocatalyst was subjected to thermal annealing in air at 300 °C for 30 min to remove any carbon enrichment or contaminants adsorbed over the photocatalyst surface as a result of the previous photocatalytic cycles.

Eventually, the photocatalyst was immersed in dichloromethane, a strong organic solvent, first for 3 min, and then for 10 min.

2.4. General Characterization of Photocatalysts

The surface morphologies and elemental compositions of the photocatalysts were characterized before use and after all 10 cycles using scanning electron microscopy (SEM) with an EVO 50VP microscope (Carl Zeiss AG, Oberkochen, Germany) equipped with a Bruker energy-dispersive X-ray spectrometer (EDS). ImageJ software (version 1.52t) was used to analyze the SEM results. The crystallographic structures of the obtained photocatalysts were analyzed by X-ray diffraction with a D2 Phaser (Bruker AXS GmbH, Karlsruhe, Germany) using Cu K radiation (λ = 1.54184 Å) in a range of 15–60°.

2.5. AFM-Raman Spectroscopy Characterization

We employed a NTEGRA Spectra system (NT-MDT), which combines atomic force microscopy (AFM) with Raman spectroscopy in an original axial configuration, to study the opaque samples. In fact, the Raman laser beam impinges on the sample on the same side where the AFM tip is placed. In our experimental system, the laser beam of the Raman setup was focused by an objective close to the apex of the AFM tip. Despite having different lateral resolutions, AFM and Raman spectroscopy can analyze the same sample area (correlation), opening the possibility of following chemical changes and possible consequences on the local morphology of the sample (or vice versa). The AFM images and Raman spectra were acquired ex situ. Particular care was devoted to the sample alignment on the stage, in view of the following changes as a function of the number of photocatalytic cycles on the same area of the sample. The AFM images were acquired in the non-contact mode using OPUS 160AC-NG Au-coated tips, (force constant = 25 N/m; resonance frequency of around 260 kHz). The tip apex was positioned in relief at the end of the cantilever; this allowed us to place the laser beam on the sample but beside the tip (displacement of about 3 µm). The Raman spectra were collected with a 532 nm laser source and a 600 line/mm grating. The scan period was between 2 and 10 s, depending on the signal intensity. The laser power applied to the pristine sample (TiO_2 nanotubes) was approximately 3 mW to avoid the formation of rutile phase [21]. Post-catalysis, the power was kept below 0.3 mW to prevent local heating and potential damage to the sample. A Nikon objective was employed for the measurements, with 100× magnification and an N.A. of 0.75.

The measurements required careful alignment of the laser beam close to the AFM tip. Generally, the former was placed at 3 µm from the latter along the axial direction of the cantilever. Being a sample-scanning system, the relative position between the AFM tip and the laser beam spot was the same during the overall acquisition process. The measurement protocol prescribed, as a first step, to acquire an AFM image of an area not smaller than (5 × 5) μm^2. As a second step, we divided this area into sub-regions with a lateral size not smaller than (0.5 × 0.5) μm^2. In the center of the sub-regions, a full Raman spectrum was acquired. This operation was repeated for each sub-region. By employing standard graphical programs, such as Origin® and MATLAB®, we could select a specific spectroscopic feature and compare its intensity for each analyzed sub-region. The normalized intensity was reported along the z-axis in a 3D graph where the X-Y plane was composed of the sub-regions of our sample. Beside each morphology image, we visualized a Raman map that represents a chemical characterization of a specific Raman feature on our sample surface.

3. Results and Discussion

3.1. Preliminary Characterization

Field emission scanning electron microscopy (FESEM) was used to analyze the starting morphologies of the photocatalysts. The top-view FE-SEM images of the photocatalysts (i.e., those that have not undergone any photocatalytic cycles) show the formation of highly ordered and regular nanotube arrays on the titanium substrate surface. In both electrodeposition conditions, silver was deposited both in the form of nanoparticles, as desired, and in larger aggregates, with more irregular shapes when an aqueous supporting electrolyte was used, and more rounded ones with the organic electrolyte (Figure 2). Yet, in the former case, at the nanoscale, the NPs appeared to be more uniformly distributed in and around the TNT mouth, with sizes ranging roughly from 40 to 100 nm (Figure 2, left). Na_2SO_4 improved the electrolyte conductivity during the deposition process, leading to a more uniform deposition of Ag NPs and preventing the clogging of Ag NPs that might accumulate at the mouths of the nanotubes during electrodeposition [22]. The Ag nanoparticles derived from the organic electrolyte (Figure 2, right) exhibited slightly larger sizes—ranging this time from 50 to 140 nm. Some nanotubes were completely closed because of the deposition of bigger nanoparticles. Ag NPs typically aggregate because of the charge differences among Ag NPs of different sizes, where smaller ones have a partial positive charge and larger ones have a partial negative charge: as a result, via the conductive substrate, larger nanoparticles tend to absorb nearby smaller particles [23,24]. The mass fraction of silver on the specimen surface was calculated instrumentally through EDX maps sampled on the representative oxide surfaces, with an approx. size of 50 μm^2. The silver fractions differed from sample to sample, consistent with the SEM images shown in Figure 2 and indicating non-optimal and non-uniform Ag distribution and formation of the agglomerates. Specifically, they were calculated to be 1.8% on sample A_UC, 2.6% on sample O_UC, and 2.7% on sample O_C.

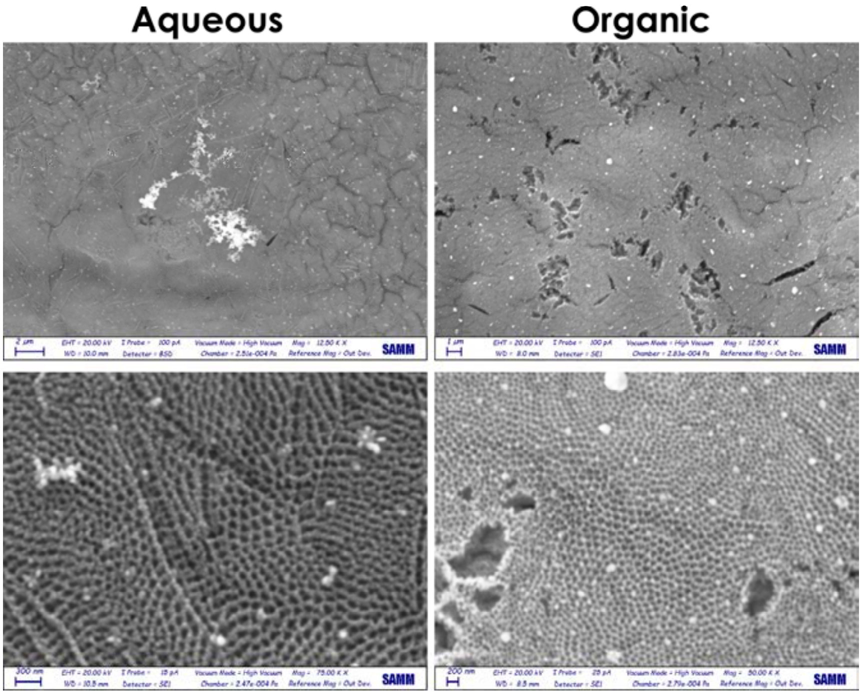

Figure 2. FESEM top-view images of Ag-decorated TNT photocatalysts, with Ag deposited from aqueous (**left**) and organic (**right**) electrolytes.

3.2. Photocatalysis Cycles

Rh-B solution degradation was used to measure the photocatalytic activity of all produced photocatalysts under UV irradiation according to the first-order kinetics, represented as follows [21]:

$$ln\frac{C}{C_0} = -kt \quad (1)$$

The apparent reaction-rate constant (k) represents the photocatalytic activity, C_0 is the initial concentration of Rh-B, and C indicates the concentration of Rh-B for different degradation times. Figure 3a shows comparative studies of the specific rate constants (the apparent reaction rate constant divided by the specific area of the photocatalyst) of the O_C and O_UC photocatalysts for all 10 photocatalytic cycles, while the photocatalytic degradation efficiency in 6 h of testing is reported in Figure 3b. Interestingly, despite the first 30% drop in photoactivity after the first use, which may be explained by partial intermediate adsorption onto the surface, in the following cycles, the photocatalyst gradually recovered its initial efficiency. The effective breaking of the conjugated structure of the RhB molecule, and thus, the effectiveness of the photocatalytic process, was confirmed by the decrease in intensity in the absorbance spectrum (inset in Figure 3a), with no peak shift, which could have indicated discoloration rather than molecule degradation. However, at the 10th cycle of use, the photocatalytic efficiency dropped significantly, indicating clear deactivation.

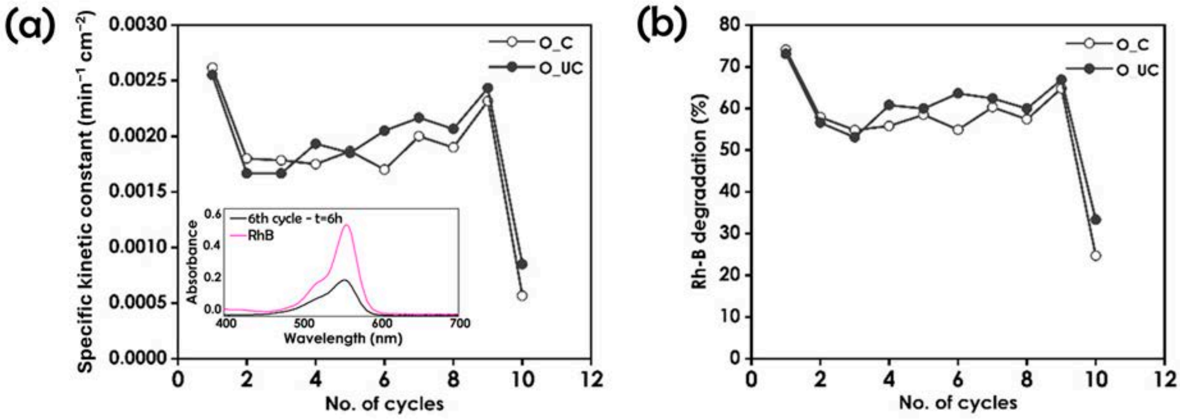

Figure 3. (**a**) Corresponding specific rate constants and (**b**) photodegradation efficiency of O_C and O_UC photocatalysts for the degradation of Rh-B under UV irradiation for 10 photocatalytic cycles. Inset in (**a**): RhB absorbance spectrum before (t = 0) and after (t = 6 h) photocatalytic test in the presence of sample O_UC used for the 6th time.

On the other hand, even after ten photocatalytic cycles, the photocatalytic activities of O_C and O_UC did not show any noticeable impact of the cleaning procedure carried out after each photocatalytic cycle on the photoactivity. Surprisingly, the uncleaned sample showed a faster recovery than the cleaned one in the long run. This may be ascribed to a slight deterioration caused by the frequent washing, which may have gradually damaged the oxide layer or partially removed the deposited silver. For this reason, in the case of the samples where silver was deposited from aqueous solution, cleaning was not performed at all (Figure 4).

While the photocatalytic efficiency was lower than that observed on the sample decorated using organic electrolyte, the sample exhibited enhanced stability. After the first 2 cycles, where a slight decrease in activity was observed, tests were conducted until the 15th cycle with no further relevant variation. These results are consistent with the SEM images captured after 10 cycles of photocatalysis (Figure 5). Indeed, sample A_UC_10 still exhibited the presence of silver nanoparticles, with the average particle size ranging between 40 and 110 nm, distributed in an ordered manner on the top of nanotubes, both inside and outside. The only difference with the pristine samples before photocatalysis was that some nanotubes were found to be covered with a few contaminants, i.e., Rh-B molecules or its partial degradation products remained adsorbed as a result of the photocatalytic tests. The lower activity with respect to O_UC may be ascribed to the smaller silver deposition extent, as proven by the previously reported EDX calculations.

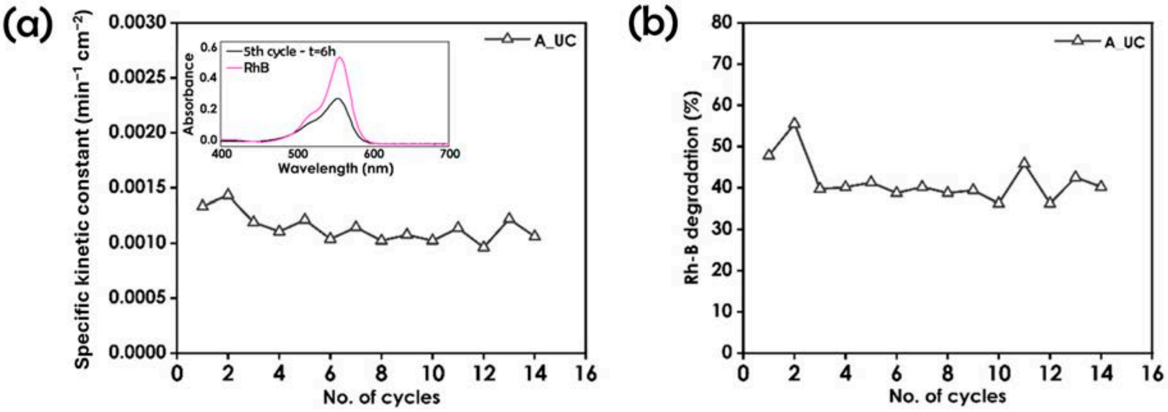

Figure 4. (**a**) Corresponding specific rate constants and (**b**) photodegradation efficiency of A_UC photocatalyst for the degradation of Rh-B under UV irradiation for 10 photocatalytic cycles. Inset in (**a**): RhB absorbance spectrum before (t = 0) and after (t = 6 h) photocatalytic test in the presence of sample A_UC used for the 5th time.

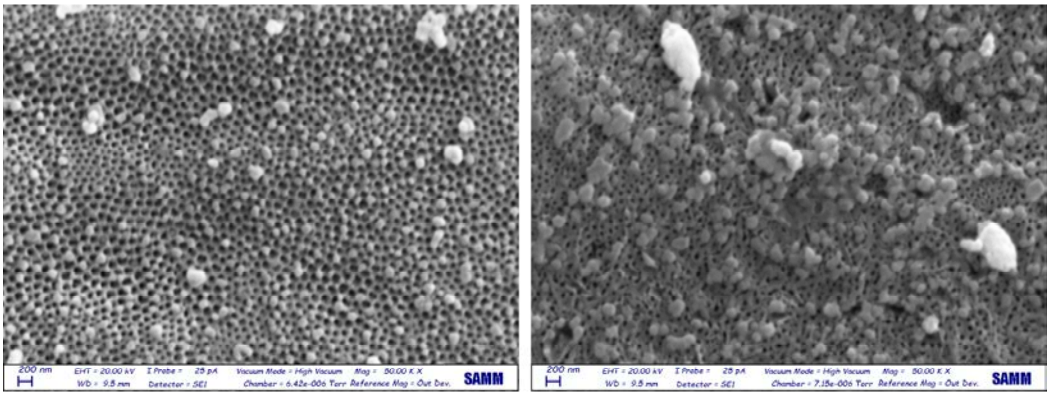

Figure 5. FESEMs of sample A_UC (**left**) and O_UC (**right**) after 10 cycles of photocatalysis.

In contrast, for the O_C and O_UC photocatalysts, their stability was compromised after nine cycles, despite the apparent absence of morphological changes (data not reported). The reasonable explanation for the drastic reduction in photoactivity could be either the deactivation caused by the reaction byproducts adsorbed on the photocatalyst surface, or the structural collapse. The SEM results support the explanation suggesting deactivation, as there were no relevant morphological changes with respect to the pristine conditions. Indeed, the surface of the nanotubes appeared less clean, with shadows on top of most nanotubes that may indicate the presence of organic residuals.

Further analyses using other characterization techniques were conducted to study the elemental composition of the adsorbed contaminants. After ten photocatalytic cycles, EDX analysis was performed (Figure 6). According to the EDX data, the elements that were most common on the surface of the photocatalysts were titanium (Ti), oxygen (O), and silver (Ag). Furthermore, residues of impurities like carbon and nitrogen were found, deriving from Rh-B residues. Although the elemental mapping shows Ag dispersed apparently uniformly over the TNT surface for each photocatalyst, with increased intensity where white particles are observed in the SEM image, this is due to the limited spatial resolution of the EDX probe. Indeed, Ag was concentrated in the nanoparticles, and not present where particles are not visible.

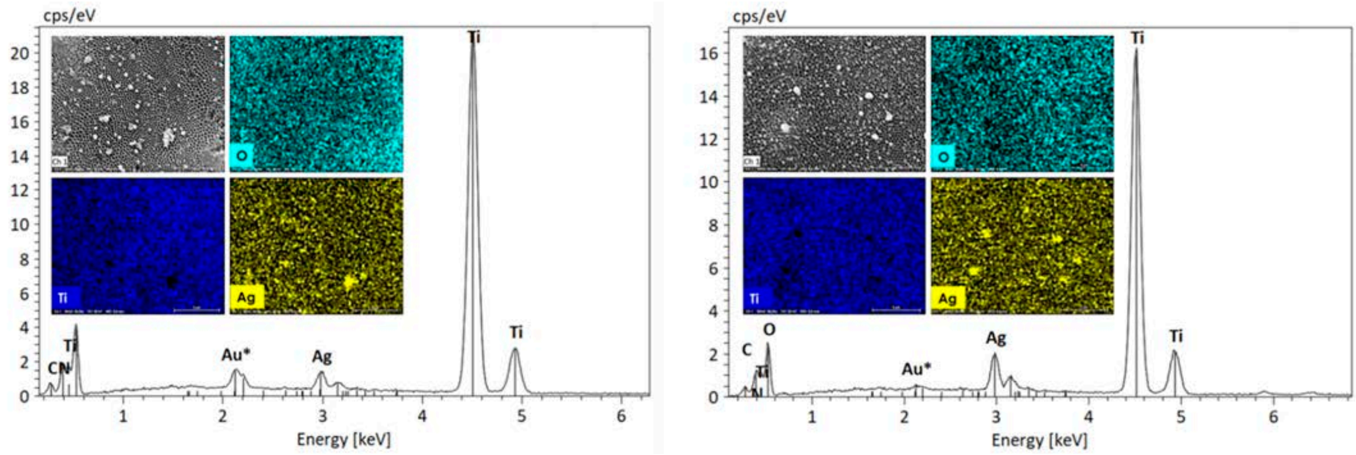

Figure 6. EDS spectra and elemental mapping images of A_UC_10 (**left**) and O_UC_10 (**right**). An asterisk marks the gold peak whose presence is due to a thin Au film deposited on the samples prior to SEM and EDS analysis. This deposition has no influence on the photoactivity investigation and is intended solely to enhance imaging quality.

Overall, it is possible to state that, from a morphological standpoint, the Ag-deposited photocatalysts under both deposition conditions remained extremely stable, exhibiting no changes even after 10 photocatalytic cycles. Furthermore, there was no apparent difference in the morphological aspects when the photocatalysts were cleaned or not. Given the absence of relevant changes observed with SEM, to confirm a possible deactivation issue, photocatalyst regeneration was carried out following the procedure described in Section 2.3.

Figure 7 reports the values of the kinetic constant obtained on sample O_UC after several attempts of surface cleaning. The first regeneration method relied on previous experience, but in the present case, gave no results. Thermal decomposition of the organic residues was not able to modify the sample conditions either. Even after immersion in dichloromethane (DCM), only a slight recovery was achieved. This implies that deactivation was not reversible.

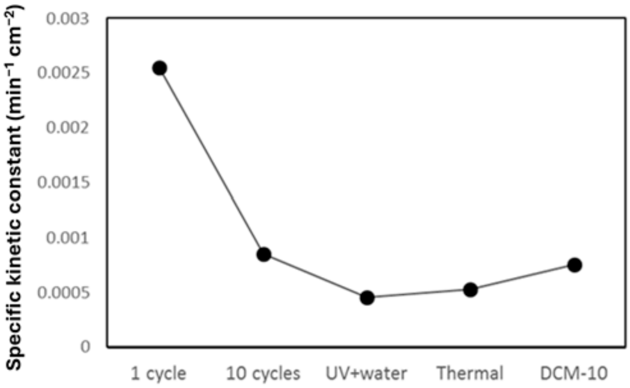

Figure 7. Specific rate constants of O_UC photocatalyst after regeneration trials.

In previous works, deactivation was found in samples similar to the ones used in the present work but for toluene removal, where sample regeneration was fully achieved. In contrast, in other works where Rh-B was used as model pollutant, no deactivation was observed, but this conclusion was drawn on a smaller number of repeated cycles [25]. This confirms that Rh-B may, with time, lead to irreversible substrate poisoning.

3.3. Coupled AFM + Raman Spectroscopy

Figure 8 reports, as an example, a tridimensional AFM image of an A-UC sample. A sensible height variation is evident, even in a relatively small area. Moreover, there are some spots with some higher particles not related to the TiO_2 nanotubes due to some clustering of the Ag nanoparticles. AFM was able to better show how the nanoparticles were integrated inside the tube openings.

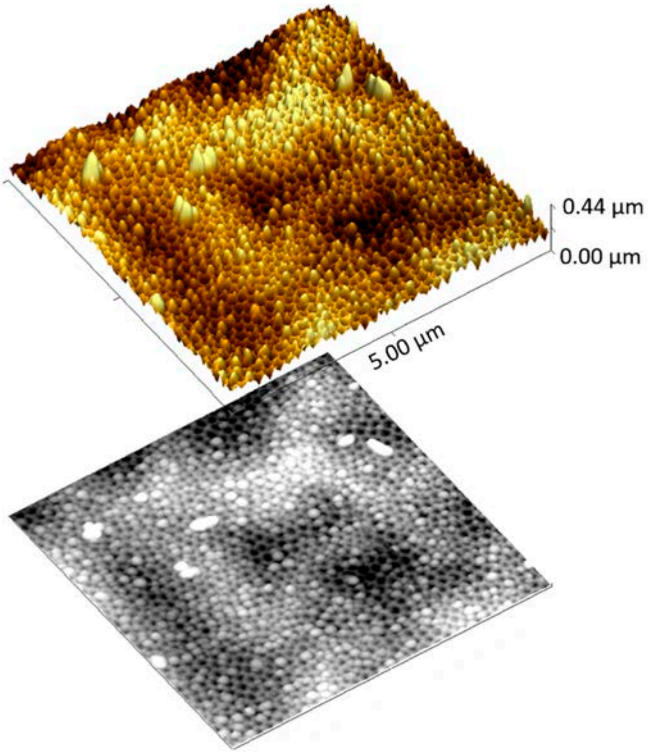

Figure 8. Three-dimensional AFM image of the A-UC sample, below in grey its 2D projection.

Comparison of the AFM and SEM images revealed an identical hexagonal morphological structure of the nanotubes, indicating that both techniques can detect the top of the aligned nanotubes characteristic of these samples.

All the samples were investigated by Raman spectroscopy. The results are reported in Figure 9. The pristine samples practically show the same spectrum, which is in very good agreement with the Raman literature on TiO_2 anatase phase [26]. We highlight the presence of a large band at around 710 cm^{-1}, which is not related to anatase phase but to the doping of the TiO_2 with Ag NPs [27]. The main peak at 144 cm^{-1} was used to construct the TiO_2 anatase map after the sample aging.

Immediately after the very first cycle (see above for details), the main spectroscopic features of TiO_2 were significantly reduced in intensity, while new intense peaks appeared at 1195 cm^{-1}, 1280 cm^{-1}, 1355 cm^{-1}, 1500 cm^{-1}, and 1640 cm^{-1}, and other less intense at 630 cm^{-1}, 760 cm^{-1}, and 930 cm^{-1}, all corresponding to the presence of Rh-B, as also reported in the literature [28,29]. By increasing the number of cycles by a factor of 10, the Raman spectra results were unaffected even though some samples (O_C_10) were washed after being used in the photocatalytic water treatment. We only observed an insignificant change in the spectrum background. This confirms that the washing procedure adopted between one photocatalysis cycle and the other was pointless and did not allow the residuals of Rh-B to be cleaned from the sample.

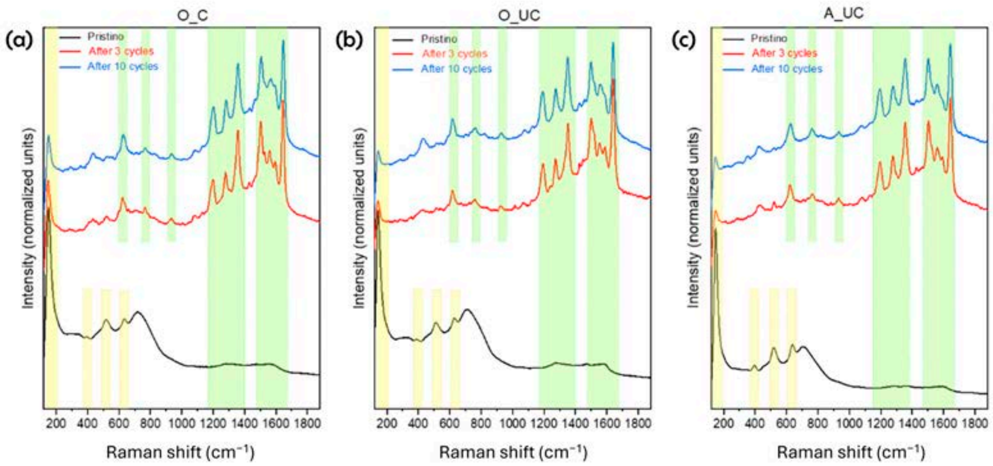

Figure 9. Raman spectra acquired on both pristine and aged samples. Panels (**b**,**c**) refer to the sample extracted from the photocatalytic cell and dried under a pure nitrogen flux. Conversely, panel (**a**) reports the data collected on the samples washed after the aging process.

It was important to check if the Raman spectroscopic features intensities, related to both the substrate and the Rh molecule, were almost uniform on the sample surface or if the concentration of Rh molecules was observed in some preferential areas of the sample. To this goal, the combined acquisition of AFM and Raman spectra was crucial to visualize the compound distribution on the surface. The results are reported in Figure 10.

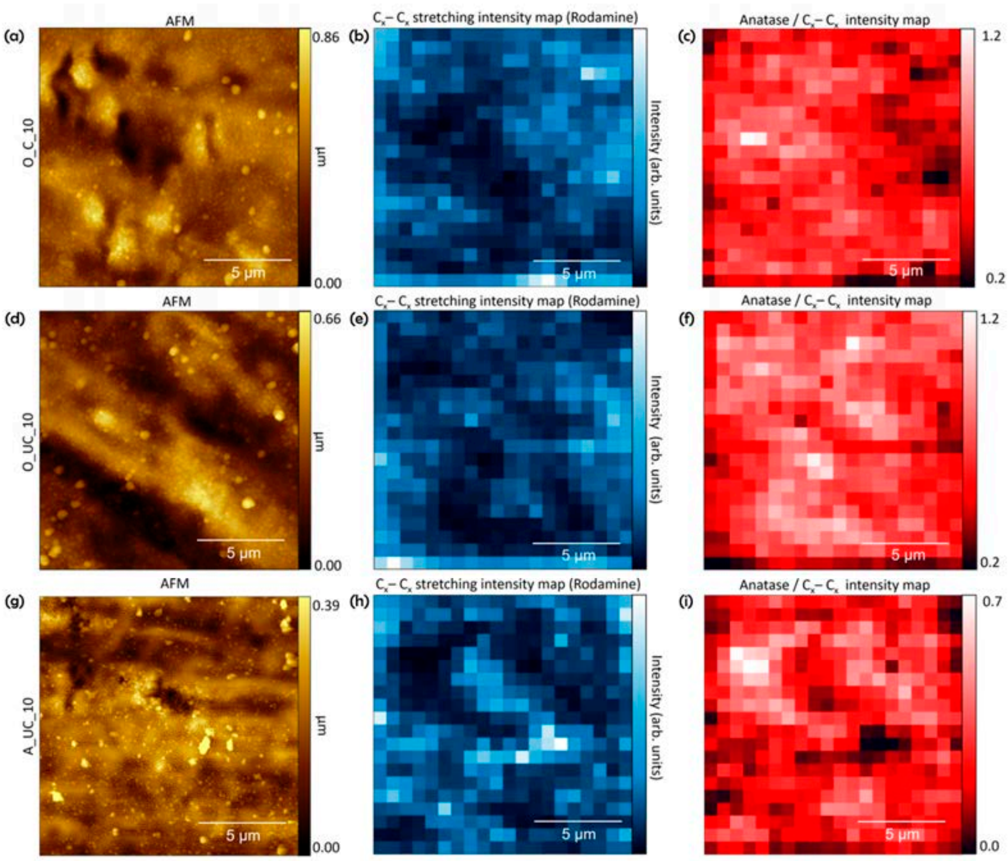

Figure 10. Morphological maps [(15 × 15) μm^2] are reported in panels (**a**,**d**,**g**), for O_C_10, O_UC_10, and A_UC_10, respectively. In the same region, the Raman intensities for Rh (namely, the Cx–Cx stretching mode, about 1640 cm^{-1}) are reported in panels (**b**,**e**,**h**). The anatase contribution (144 cm^{-1}) map is shown in panels (**c**,**f**,**i**).

The AFM morphologies (Figure 10a,d) showed some more roundish clusters on the sample surface with respect to the pristine ones. This effect was a direct consequence of the progressive aging of the sample. The scanned area was divided into sub-regions with a lateral size of about 750 nm, where the Raman spectrum was collected (see Materials and Methods section). The intensities are reported in the other panels of the image. The Rh-B molecule contribution (peak selected at about 1640 cm^{-1}) is shown in panels (b) and (e). The molecule was apparently distributed quite uniformly on O_C_10 and O_UC_10, although the Raman signal minima are aligned with the hollows shown in the surface morphology in the corresponding AFM maps. The anatase signal contribution (panels (c) and (f)) found its maximum intensity in the regions where the Rh-B signal was at a minimum. Thus, the chemical maps, together with the AFM morphologies, suggest a sudden surface coverage by Rh-B after the first photocatalytic cycle, which, however, can be partially affected by the local quality of the surface morphology (e.g., hills, hollow regions, etc.). Analogous comments are also valid for sample A_UC_10.

To better highlight this correlation, Figure 11 reports the AFM (panel (a)) and Raman spectroscopy (panel (c)) overlapping (panel (b)). As previously mentioned, it can be seen that where more round-shape features are present, i.e., Ag particle clusters, there is a brighter area in the Rh-B Raman intensity map.

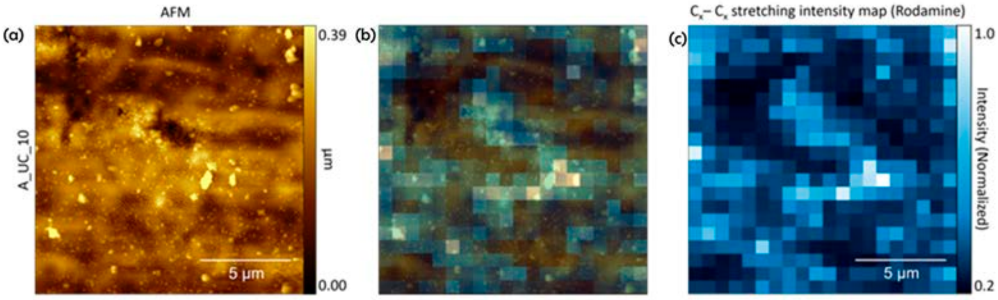

Figure 11. (**a**) AFM morphology; (**c**) Raman intensity map of the C_x–C_x stretching intensity map; (**b**) overlapping of panels (**a**,**c**).

In conclusion, the AFM-Raman correlation developed and demonstrated in this study represents a significant advancement in the analysis of real surfaces, particularly those with notable roughness and complex topographies. Unlike more simplified model systems, such as single crystals, which exhibit uniform and idealized characteristics, real-world materials often present intricate surface irregularities. The combination of AFM and Raman spectroscopy not only allows for a more precise mapping of these surface features but also offers a deeper and more comprehensive understanding of the chemical and physical properties of such materials. This enhanced level of detail is particularly valuable for studying surfaces with practical applications, where the interaction between the surface morphology and material behavior is critical. By integrating these two powerful techniques, we are better equipped to tackle the challenges associated with analyzing more complex and realistic systems.

4. Conclusions

In this study, we have successfully demonstrated the integration of atomic force microscopy (AFM) and Raman spectroscopy to investigate the photoactivity of Ag-decorated TiO_2 nanotube arrays. This combined approach allowed us to explore both the morphological and chemical changes in the photocatalytic substrates, offering a more comprehensive understanding of the degradation and deactivation mechanisms occurring after multiple photocatalytic cycles. Our findings indicate that the samples where Ag was electrodeposited from an organic electrolyte showed significant performance deterioration after 10 cycles, and traditional cleaning methods were ineffective in restoring their photocatalytic activity.

Moreover, the proposed coupling of AFM microscopy with Raman spectroscopy suggests a broader field of investigation and expands the possibilities for the chemical mapping of real-world samples. This method proves particularly valuable for samples with substantial surface roughness, which might hinder the application of more sophisticated techniques. In such contexts, our combined setup offers a practical and effective solution for surface analysis.

In the future, we plan to further enhance the setup by implementing in situ sample illumination directly within the AFM-Raman measurement cell. This addition will enable the real-time monitoring of photocatalytic processes, potentially offering new insights into the deactivation mechanisms of certain materials. We believe that these advancements will open up exciting opportunities for future research, providing deeper interpretations of the material behavior under operational conditions.

Author Contributions: M.V.S. and M.M equally contributed to this work. Conceptualization, M.V.D. and G.B.; methodology, M.V.D. and G.B.; validation, L.D. and M.P.; formal analysis, M.V.S. and M.M.; investigation, M.V.S. and M.M.; resources, G.B.; data curation, M.V.S. and M.M.; writing—original draft preparation, M.V.S. and M.M.; writing—review and editing, M.V.D., G.B., L.D., and M.P.; visualization, M.V.D.; supervision, L.D. and M.P. All authors have read and agreed to the published version of the manuscript.

Funding: This study was carried out within the MICS (Made in Italy—Circular and Sustainable) Extended Partnership and received funding from the European Union Next–Generation EU (PIANO NAZIONALE DI RIPRESA E RESILIENZA (PNRR) MISSIONE 4 COMPONENTE 2, INVESTIMENTO 1.3—D.D 1551.11-10-2022, PE00000004).

Data Availability Statement: The data are available upon request.

Acknowledgments: The authors are grateful to Elia Mazzoletti (Politecnico di Milano) for the preparation of the MATLAB® codes.

Conflicts of Interest: The authors declare no conflicts of interest.

References

1. Choi, H.; Zakersalehi, A.; Al-Abed, S.R.; Han, C.; Dionysiou, D.D. Nanostructured Titanium Oxide Film- and Membrane-Based Photocatalysis for Water Treatment. In *Nanotechnology Applications for Clean Water*; William Andrew Publishing: Norwich, NY, USA, 2014; pp. 123–132.
2. Koukkari, P.; Pajarre, R.; Hack, K. Modelling TiO_2 Production by Explicit Use of Reaction Kinetics. In *The SGTE Casebook*; Woodhead Publishing: Cambridge, UK, 2008; pp. 437–446.
3. Mao, T.; Zha, J.; Hu, Y.; Chen, Q.; Zhang, J.; Luo, X. Research Progress of TiO_2 Modification and Photodegradation of Organic Pollutants. *Inorganics* **2024**, *12*, 178. [CrossRef]
4. Yan, X.; Chen, X. Titanium Dioxide Nanomaterials. In *Encyclopedia of Inorganic and Bioinorganic Chemistry*; John Wiley & Sons: Hoboken, NJ, USA, 2015; pp. 1–38.
5. Li, R.; Zhou, A.; Lu, Q.; Yang, C.; Zhang, J. In Situ Monitoring and Analysis of the Photocatalytic Degradation Process and Mechanism on Recyclable Au NPs-TiO_2 NTs Substrate Using Surface-Enhanced Raman Scattering. *Colloids Surf. A. Physicochem. Eng. Asp.* **2013**, *436*, 270–278. [CrossRef]
6. Wint, T.H.M.; Smith, M.F.; Chanlek, N.; Chen, F.; Oo, T.Z.; Songsiriritthigul, P. Physical Origin of Diminishing Photocatalytic Efficiency for Recycled TiO_2 Nanotubes and Ag-Loaded TiO_2 Nanotubes in Organic Aqueous Solution. *Catalysts* **2020**, *10*, 737. [CrossRef]
7. Chong, X.; Zhao, B.; Li, R.; Ruan, W.; Yang, X. Photocatalytic Degradation of Rhodamine 6G on Ag Modified TiO_2 Nanotubes: Surface-Enhanced Raman Scattering Study on Catalytic Kinetics and Substrate Recyclability. *Colloids Surf. A. Physicochem. Eng. Asp.* **2015**, *481*, 7–12. [CrossRef]
8. de Oliveira, R.; Sant'Ana, A.C. Plasmonic Photocatalytic Degradation of Tebuconazole and 2,4-Dichlorophenoxyacetic Acid by Ag Nanoparticles-Decorated TiO_2 Tracked by SERS Analysis. *Chemosphere* **2023**, *338*, 139490. [CrossRef]
9. Xie, Y.; Jin, Y.; Zhou, Y.; Wang, Y. SERS Activity of Self-Cleaning Silver/Titania Nanoarray. *Appl. Surf. Sci.* **2014**, *313*, 549–557. [CrossRef]
10. Székely, I.; Kovács, Z.; Rusu, M.; Gyulavári, T.; Todea, M.; Focșan, M.; Baia, M.; Pap, Z. Tungsten Oxide Morphology-Dependent Au/TiO_2/WO_3 Heterostructures with Applications in Heterogenous Photocatalysis and Surface-Enhanced Raman Spectroscopy. *Catalysts* **2023**, *13*, 1015. [CrossRef]
11. Piazza, V.; Mazare, A.; Diamanti, M.V.; Pedeferri, M.; Schmuki, P. Key Oxidation Parameters That Influence Photo-Induced Properties and Applications of Anodic Titanium Oxides. *J. Electrochem. Soc.* **2016**, *163*, H119–H127. [CrossRef]

12. Wang, Y.; Zhang, M.; Yu, H.; Zuo, Y.; Gao, J.; He, G.; Sun, Z. Facile Fabrication of Ag/Graphene Oxide/TiO_2 Nanorod Array as a Powerful Substrate for Photocatalytic Degradation and Surface-Enhanced Raman Scattering Detection. *Appl. Catal. B.* **2019**, *252*, 174–186. [CrossRef]
13. Serrano, G.; Bonanni, B.; Kosmala, T.; Di Giovannantonio, M.; Diebold, U.; Wandelt, K.; Goletti, C. In situ scanning tunneling microscopy study of Ca-modified rutile TiO_2(110) in bulk water. *Beilstein J. Nanotechnol.* **2015**, *6*, 438–443. [CrossRef]
14. Diamanti, M.V.; Gadelrab, K.R.; Pedeferri, M.P.; Stefancich, M.; Pehkonen, S.O.; Chiesa, M. Nanoscale Investigation of Photoinduced Hydrophilicity Variations in Anatase and Rutile Nanopowders. *Langmuir* **2013**, *29*, 14512–14518. [CrossRef] [PubMed]
15. Verma, P. Tip-Enhanced Raman Spectroscopy: Technique and Recent Advances. *Chem. Rev.* **2017**, *117*, 6447–6466. [CrossRef] [PubMed]
16. Zeng, Z.-C.; Huang, S.-C.; Wu, D.-Y.; Meng, L.-Y.; Li, M.-H.; Huang, T.-X.; Zhong, J.-H.; Wang, X.; Yang, Z.-L.; Ren, B. Electrochemical Tip-Enhanced Raman Spectroscopy. *J. Am. Chem. Soc.* **2015**, *137*, 11928–11931. [CrossRef] [PubMed]
17. Bussetti, G.; Menegazzo, M.; Mitko, S.; Castiglioni, C.; Tommasini, M.; Lucotti, A.; Magagnin, L.; Russo, V.; Li Bassi, A.; Siena, M.; et al. A Combined Raman Spectroscopy and Atomic Force Microscopy System for In Situ and Real-Time Measures in Electrochemical Cells. *Materials* **2023**, *16*, 2239. [CrossRef] [PubMed]
18. Pishkar, N.; Ghoranneviss, M.; Ghorannevis, Z.; Akbari, H. Study of the Highly Ordered TiO_2 Nanotubes Physical Properties Prepared with Two-Step Anodization. *Results Phys.* **2018**, *9*, 1246–1249. [CrossRef]
19. Montakhab, E.; Rashchi, F.; Sheibani, S. Modification and Photocatalytic Activity of Open Channel TiO_2 Nanotubes Array Synthesized by Anodization Process. *Appl. Surf. Sci.* **2020**, *534*, 147581. [CrossRef]
20. Ng, S.W.; Yam, F.K.; Hassan, Z. Electrochemical Impregnation of Silver Nanostructures in Titanium Dioxide Nanotubes. *J Electrochem. Soc.* **2012**, *159*, D742–D746. [CrossRef]
21. Depero, L.E.; Bonzi, P.; Zocchi, M.; Casale, C.; De Michele, G. Study of the Anatase-Rutile Transformation in TiO_2 Powders Obtained by Laser-Induced Synthesis. *J. Mater. Res.* **1993**, *8*, 2709–2715. [CrossRef]
22. Redmond, P.L.; Hallock, A.J.; Brus, L.E. Electrochemical Ostwald Ripening of Colloidal Ag Particles on Conductive Substrates. *Nano. Lett.* **2005**, *5*, 131–135. [CrossRef]
23. Nycz, M.; Arkusz, K.; Pijanowska, D.G. Fabrication of Electrochemical Biosensor Based on Titanium Dioxide Nanotubes and Silver Nanoparticles for Heat Shock Protein 70 Detection. *Materials* **2021**, *14*, 3767. [CrossRef]
24. Zakaria, N.D.; Omar, M.H.; Ahmad Kamal, N.N.; Abdul Razak, K.; Sönmez, T.; Balakrishnan, V.; Hamzah, H.H. Effect of Supporting Background Electrolytes on the Nanostructure Morphologies and Electrochemical Behaviors of Electrodeposited Gold Nanoparticles on Glassy Carbon Electrode Surfaces. *ACS Omega* **2021**, *6*, 24419–24431. [CrossRef] [PubMed]
25. Bellè, U.; Spini, D.; Del Curto, B.; Pedeferri, M.; Diamanti, M.V. Water-Based Photocatalytic Sol–Gel TiO_2 Coatings: Synthesis and Durability. *Catalysts* **2023**, *13*, 494. [CrossRef]
26. Zhang, W.F.; He, Y.L.; Zhang, M.S.; Yin, Z.; Chen, Q. Raman Scattering Study on Anatase TiO_2 Nanocrystals. *J. Phys. D. Appl. Phys.* **2000**, *33*, 912–916. [CrossRef]
27. Lim, S.P.; Pandikumar, A.; Lim, H.N.; Ramaraj, R.; Huang, N.M. Boosting Photovoltaic Performance of Dye-Sensitized Solar Cells Using Silver Nanoparticle-Decorated N,S-Co-Doped-TiO_2 Photoanode. *Sci. Rep.* **2015**, *5*, 11922. [CrossRef]
28. Sun, C.H.; Wang, M.L.; Feng, Q.; Liu, W.; Xu, C.X. Surface-Enhanced Raman Scattering (SERS) Study on Rhodamine B Adsorbed on Different Substrates. *Russ. J. Phys. Chem. A* **2015**, *89*, 291–296. [CrossRef]
29. Majoube, M.; Henry, M. Fourier Transform Raman and Infrared and Surface-Enhanced Raman Spectra for Rhodamine 6G. *Spectrochim. Acta A* **1991**, *47*, 1459–1466. [CrossRef]